Front. Struct. Civ. Eng. 2021, 15(5): 1144–1159
https://doi.org/10.1007/s11709-021-0762-4

RESEARCH ARTICLE

Axial compression behavior of CFRP-confined rectangular concrete-filled stainless steel tube stub column

Hongyuan TANG[a*], Ruizhong LIU[a], Xin ZHAO[a], Rui GUO[a], Yigang JIA[b]

[a] *Institute of Structural Engineering, Xihua University, Chengdu 610039, China*
[b] *Institute of Design and Research, Nanchang University, Nanchang 330029, China*
[*] *Corresponding author. E-mail: tanghyseu@163.com*

ABSTRACT The mechanical properties of CFRP-confined rectangular concrete-filled stainless steel tube (CFSST) stub columns under axial compression were experimentally studied. A total of 28 specimens (7 groups) were fabricated for the axial compression test to study the influences of length-to-width ratio, CFRP constraint coefficient, and the thickness of stainless steel tube on the axial compression behavior. The specimen failure modes, the stress development of stainless steel tube and CFRP wrap, and the load–strain ratio curves in the loading process were obtained. Meanwhile, the relationship between axial and transverse deformations of each specimen was analyzed through the typical relative load−strain ratio curves. A bearing capacity prediction method was proposed based on the twin-shear strength theory, combining the limit equilibrium state of the CFRP-confined CFSST stub column under axial compression. The prediction method was calibrated by the test data in this study and other literature. The results show that the prediction method is of high accuracy.

KEYWORDS CFRP, rectangular CFSST stub column, bearing capacity, limit equilibrium state, twin-shear strength theory

1 Introduction

Carbon fiber reinforced polymer (CFRP) has been extensively applied to the engineering construction and reinforcement of damaged structures due to its high specific strength (ratio of tensile strength to density). The present studies on CFRP-confined concrete-filled columns and steel tube columns mainly were concentrated on the columns with circular sections.

Compared with a circular cross-section column, a rectangular cross-section (square one included) column can easily simplify the joint in the design, which can effectively expedite the construction progress. Some scholars had conducted experimental studies on CFRP-confined rectangular concrete-filled steel tube (CFST) stub columns. The results revealed that the strength and ductility of the CFRP-confined rectangular CFST stub column were improved to a certain extent [1]. Marques et al. [2], Jiang and Teng [3], Masia et al. [4], Guo et al. [5], Wang and Wu [6], Ozbakkaloglu [7], and Yang et al. [8] conducted numerous experiments. They systematically studied the failure mechanism of CFRP-confined rectangular CFST, CFRP constraint mechanism, and the influences of chamfer radius, sectional length-to-width ratio, CFRP and concrete material type, and the constraint coefficient on the bearing capacity of stub columns. The prediction models for ultimate bearing capacity considering slenderness ratio and size effect were proposed as well. Meanwhile, Tao et al. [9,10], Wang et al. [11], Dong et al. [12], Sundarraja and Prabhu [13] conducted axial compression tests on CFRP-confined rectangular CFST tube columns. However, the corrosion resistance of conventional carbon steel tubes is poor. Rusting, strength reduction and even member failure may be easily generated under long-term corrosion. Replacing conventional carbon steel with stainless steel of strong

Article history: Received May 27, 2021; Accepted Jun 20, 2021

corrosion resistance to constitute stainless steel tube and concrete composite structures has become a focus of research worldwide. Zhou et al. [14] studied the behavior of stainless steel stub columns under cyclic loading. The global and local buckling behaviors of stainless steel members were analyzed. Fang et al. [15] provided a new method for evaluating the ductility of stainless steel RHSs / SHSs under different loads. Young and Ellobody [16], and Uy et al. [17] conducted axial compression tests on CFSST stub columns. The result indicated that CFSST stub columns had a higher bearing capacity and ductility than CFST stub columns and had favorable mechanical properties and application prospects. Considering the shape of cross-section and concrete type as the variables, Ibañez et al. [18] studied the influence of concrete strength on the ultimate bearing capacity of columns and found that the prediction effect of the existing standards on the bearing capacity was inaccurate.

The CFSST has broad application prospects in the marine environment. However, the current research shows that in the marine environment with high chloride ion content, the stainless steel would also undergo pitting corrosion, which would cause local corrosion and influence the performance of the structure. The CFRP provides a new choice for its anti-corrosion. The use of CFRP can significantly increase the bearing capacity without changing the thickness of stainless steel, which reduces the amount of stainless steel. Tang et al. [19] conducted an experimental study of axial compression behaviors of CFRP-confined circular CFSST stub columns. However, the axial compression behavior of CFRP-confined rectangular CFSST stub column has not been investigated.

To study the axial compression behavior of the CFRP-confined rectangular CFSST stub column, a total of seven rectangular CFSST stub columns and 21 CFRP-confined rectangular CFSST stub columns were tested under axial loading. The influences of the length-to-width ratio, wall thickness of stainless steel tube, and CFRP constraint effect on the bearing capacity were discussed. A prediction model was proposed for the bearing capacity of the CFRP-confined rectangular CFSST stub column.

2 Test profile

2.1 Specimen design

Figure 1 shows the specimens tested in this study, where H and B are long and short sides of the cross-section of stainless steel tube, respectively. The main parameters included length-to-width ratio (H/B), constraint coefficient (ξ_s) of stainless steel tube, and constraint coefficient (ξ_{fr}) of CFRP. The thickness (t_{fr}) of a single-layer CFRP is 0.17 mm. For all specimens, the height-to-width ratio was taken as 3, namely, $L = 3H = 360$ mm. The specimen numbers and main parameters are shown in Table 1. According to the cross-sectional form and the constraint effect of stainless steel tube, the specimens were divided into groups RA, RB, RC, RD, SA, SB, and SC, where the initials 'R' and 'S' represent rectangular and square, respectively, the letters 'A'–'D' are used to distinguish the specimens with different stainless steel tube constraint effects, and the Arabic numeral at the end represents the number of CFRP layers.

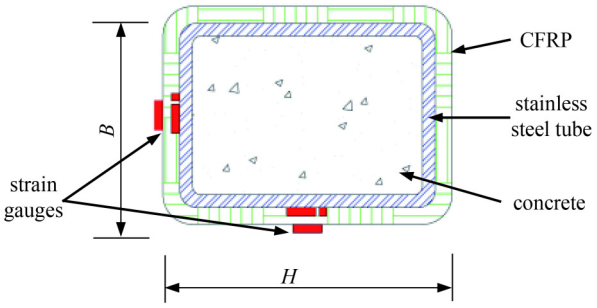

Fig. 1 Cross section of specimen.

The stainless steel tube constraint effect coefficient (ξ_s) and CFRP constraint effect coefficient (ξ_{fr}) are respectively calculated through the following equations:

$$\xi_s = A_s\sigma_{0.2}/(0.67A_c f_{cu}), \tag{1}$$

$$\xi_{fr} = A_{fr}f_{fr}/(0.67A_c f_{cu}), \tag{2}$$

where A_s and $\sigma_{0.2}$ denote the cross-sectional area and nominal yield strength of stainless steel tube, respectively; A_c is the cross-sectional areas of the core concrete; f_{cu} denotes the cubic compressive strength of the concrete; A_{fr} and f_{fr} present the cross-sectional area and ultimate tensile strength of CFRP, respectively.

2.2 Material properties

Rectangular seamless Austenitic 304 stainless steel tubes were used in the test, the internal chamfer radius was the same as the wall thickness, and the tensile test of the stainless steel was conducted in accordance with Chinese Standard GB/T228.1–2010 [20]. The material properties of stainless steel were listed in Table 2. The hardening index n can be calculated as follows:

$$n = \frac{\ln 20}{\ln(\sigma_{0.2}/\sigma_{0.01})}, \tag{3}$$

where $\sigma_{0.2}$ and $\sigma_{0.01}$ denote the nominal yield strength and 0.01% proof stress.

Ordinary Portland cement with a design strength grade of 52.5 and coarse aggregate with a maximum particle size of 18 mm were used to prepare the concrete. After 28 d

Table 1 Parameters of specimens

specimen	section size (mm)	H/B	L (mm)	t_s (mm)	n_f	t_{fr} (mm)	ξ_s	ξ_{fr}	N_u (kN)
RA0	120 × 60	2.0	360	4	0	0.00	4.31	0.000	1261
RA1	120 × 60	2.0	360	4	1	0.17	4.31	0.667	1391
RA2	120 × 60	2.0	360	4	2	0.34	4.31	1.334	1412
RA3	120 × 60	2.0	360	4	3	0.51	4.31	2.001	1478
RB0	120 × 60	2.0	360	5	0	0.00	6.09	0.000	1632
RB1	120 × 60	2.0	360	5	1	0.17	6.09	0.706	1728
RB2	120 × 60	2.0	360	5	2	0.34	6.09	1.412	1816
RB3	120 × 60	2.0	360	5	3	0.51	6.09	2.118	1899
RC0	120 × 80	1.5	360	4	0	0.00	3.33	0.000	1362
RC1	120 × 80	1.5	360	4	1	0.17	3.33	0.482	1453
RC2	120 × 80	1.5	360	4	2	0.34	3.33	0.964	1612
RC3	120 × 80	1.5	360	4	3	0.51	3.33	1.446	1786
RD0	120 × 80	1.5	360	5	0	0.00	4.67	0.000	1732
RD1	120 × 80	1.5	360	5	1	0.17	4.67	0.505	1821
RD2	120 × 80	1.5	360	5	2	0.34	4.67	1.010	1921
RD3	120 × 80	1.5	360	5	3	0.51	4.67	1.515	2008
SA0	120 × 120	1.0	360	4	0	0.00	2.76	0.000	1815
SA1	120 × 120	1.0	360	4	1	0.17	2.76	0.740	1946
SA2	120 × 120	1.0	360	4	2	0.34	2.76	1.480	2054
SA3	120 × 120	1.0	360	4	3	0.51	2.76	2.220	2127
SB0	120 × 120	1.0	360	5	0	0.00	3.73	0.000	2275
SB1	120 × 120	1.0	360	5	1	0.17	3.73	0.770	2388
SB2	120 × 120	1.0	360	5	2	0.34	3.73	1.540	2488
SB3	120 × 120	1.0	360	5	3	0.51	3.73	2.300	2615
SC0	120 × 120	1.0	360	6	0	0.00	4.71	0.000	2854
SC1	120 × 120	1.0	360	6	1	0.17	4.71	0.800	2952
SC2	120 × 120	1.0	360	6	2	0.34	4.71	1.590	3032
SC3	120 × 120	1.0	360	6	3	0.51	4.71	2.390	3279

Note: t_s is the wall thickness of stainless steel tube, and n_f denote the number of CFRP layers.

Table 2 Material properties of stainless steel

section size (mm)	$\sigma_{0.2}$ (MPa)	E_0 (GPa)	n
120 × 60 × 4	538	195	5
120 × 60 × 5	581	200	4
120 × 80 × 4	516	196	5
120 × 80 × 5	558	200	5
120 × 120 × 4	549	203	5
120 × 120 × 5	578	203	5
120 × 120 × 6	598	203	5

of curing under standard curing conditions, the compressive strength of concrete was measured according to Chinses standard GB/T50080−2016 [21], and the cubic compressive strength was 43.96 MPa. The two ends of the CFSST stub column were ground with a grinder to ensure smooth enough that the stainless steel tube and the core concrete can work together under the axial loading.

The carbon fiber sheet CFS-I-300 and the adhesive used in the test were consistent with Ref. [22]. The elasticity modulus of the adhesive is 2.49 GPa, and the tensile strength is 53.1 MPa. The detailed CFRP parameters are presented in Table 3.

Table 3 Material properties of CFRP

material	E_{fr} (GPa)	υ	f_{fr} (MPa)
CFRP	243	0.2	3418

Note: E_{fr} is the elastic modulus of CFRP sheet; υ presents the Poisson's ratio; and f_{fr} is the tensile strength of CFRP sheet.

2.3 Loading and measurement

A 5000 kN servo-hydraulic was used in the experiment. The loading rate was 0.6 mm/min. The experiments were terminated when the axial displacement reached 25 mm. Transverse strain gauges were arranged on the CFRP surface to measure the CFRP strain, and the relative arrangement position was consistent with the transverse strain gauge of the steel tube, as shown in Fig. 2(a). A total of 12 transverse and longitudinal strain gauges were arranged on two adjacent planes (Fig. 2(b)) to measure the stainless steel tube deformation. Meanwhile, three LVDTs were placed around each specimen (Fig. 2(c)) to measure the longitudinal displacement. The test data were recorded with a static data acquisition system.

3 Test results and discussions

3.1 Test phenomena

No deformation was present on the control specimens without CFRP in the initial loading stage. The bulging of stainless steel tubes was generated at 1/4 and 3/4 of the height of the H-plane of most specimens (Fig. 3(a)) when the load was increased to approximately $0.95N_u$. The bulging degree on plane H was elevated as the load continued to rise. Moreover, the buckling phenomenon emerged on plane B; the 'elephant foot'-shaped buckling phenomenon was generated due to buckling at the upper or lower ends of the specimen (Fig. 3(b)).

The test phenomenon of CFRP-confined specimens was similar to that of the control specimens in the initial loading stage. None of the specimens occurred deformation in the initial loading stage. The bulging phenomenon appeared at 1/4 and 3/4 of the height of the H-plane of most specimens (Fig. 3(c)) when the load increased to approximately $0.9N_u$. The CFRP at the chamfer, which was at the same height as the specimen bulging part, was suddenly broken (Fig. 3(d)) when the load reached N_u. The continuous explosive sound was generated, and the bearing capacity of the specimen also dropped.

The CFRP was peeled off the CFSST after the end of the experiment. Taking the specimens with sectional size 120 mm × 60 mm as an example (Fig. 3(e)), the buckling phenomenon appeared at the same position at the lower end of the CFRP-confined CFSST stub column. The wrinkle at the upper end of the member was gradually shifted downward and reduced as the number of CFRP

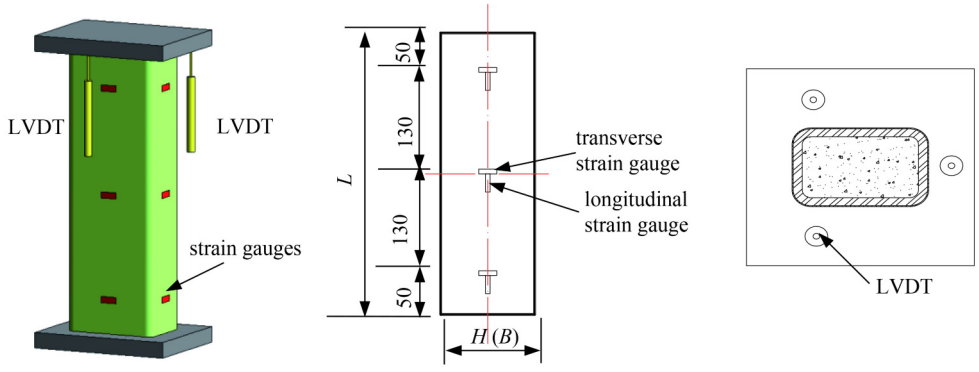

Fig. 2 Strain gauges and measurement layout: (a) arrangement of strain gauges on CFRP; (b) arrangement of strain gauges on stainless steel tube; (c) arrangement of LVDTs.

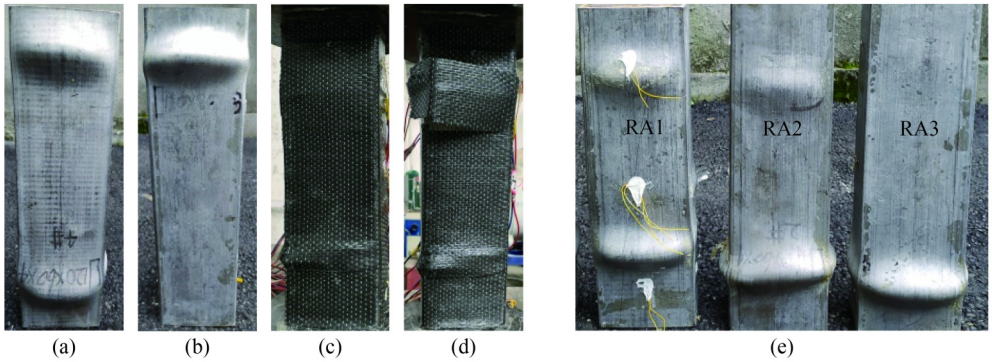

Fig. 3 Failure modes: (a) RA0; (b) RC0; (c) RA1; (d) RA1; (e) final failure modes after peeling off CFRP.

layers increased, indicating that CFRP could effectively postpone the local buckling of the CFSST columns.

3.2 Load-strain curves

The development trends of transverse strains on the stainless steel tube agree well with those of CFRP, as illustrated in Fig. 4. Thus, CFRP constrained the stainless steel tube well before the rupture of CFRP, and their deformations were synchronous.

The values measured by strain gauges and displacement meters were used as the strain data of the specimens before and after the CFRP failure, respectively. The load−axial shortening curve is similar to the load−axial strain curve. The load–strain curves of CFRP-confined rectangular CFSST stub columns were reported in Figs. 5(a)–5(g). The typical load–strain curve is shown in Fig. 5(h), divided into four stages: elastic stage *OA*, elastic-plastic stage *AB*, CFRP failure stage *BC*, and residual stage *CD* (*CE* or *CF*). The residual stage of the specimen with different cross-sections and constraint effects presents different characteristics. The detailed analysis was as follows.

1) Elastic stage *OA*

The elastic deformation of specimens occurred during the initial loading stage, and an approximately linear relationship between the load and the strain was obtained. Because CFRP has no effective restraint effect on CFSST in this stage, the curves of different specimens were almost coincident.

2) Elastic–plastic stage *AB*

The slight deformation of the specimen appeared with the increase of the load, which came into the elastic−plastic phase. The load−strain curve is smooth and nonlinear, and the absolute value of the curve slope of the CFRP-confined specimens was gradually larger than that of the control specimens. The effective constraint generated by CFRP on the stainless steel tube was gradually enlarged, and the stiffness and bearing capacity of the specimen increased. When the load reached $0.9N_u$, the apparent bulging deformation of the specimen was present, and the curve tended to be flat. The continuous cracking sound was generated when the load was increased to N_u.

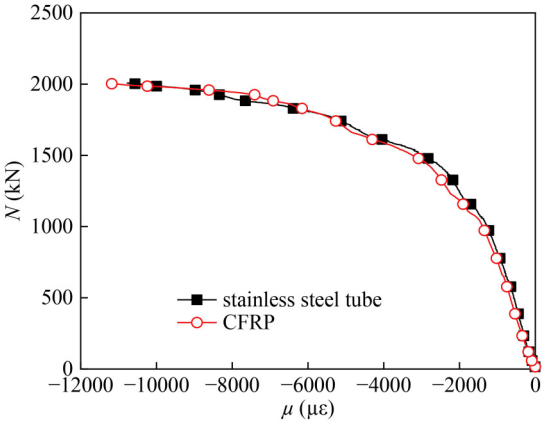

Fig. 4 Load–strain relationship of CFRP and tube.

3) CFRP failure stage *BC*

When the load reached N_u, the CFRP at the chamfer, which was at the same height as the specimen bulging part, was suddenly broken, and the load−strain curve suddenly dropped. Within a small segment of the follow-up strain zone, the curve further declined as the CFRP burst within a small scope, but the decreased amplitude was reduced.

4) Descent stage *CD*

The bending phenomenon of the specimens in RA and RB groups was present, and the load−strain curve decreased the specimens in the SA group with small steel tube constraint effects. However, the load declined slowly, and the specimens presented ductile failure.

5) Ideal plastic stage *CE*

A sufficient restraining force was provided to the core concrete for the RC2 and the specimens in SB and SC groups. Therefore, the specimens entered the ideal plastic stage due to the considerable stainless steel tube constraint effect after the CFRP failure.

6) Hardening stage *CF*

For RC1, RC3, and the specimens in groups RD, the tightening force was mainly due to the substantial stainless steel tube constraint effect and the entrance of stainless steel tube into the plastic hardening stage. Thus, the hardening stage would appear after the CFRP failure stage.

The curve development trends of the control group and the corresponding CFRP-confined specimens were identical after the CFRP broke. This phenomenon indicates that the stress state of the CFRP-confined rectangular CFSST stub columns was consistent with that of the control group.

3.3 Relative load (N/N_u) –strain ratio (ν) relation curves

The constraint effect of stainless steel tube on core concrete can be further investigated using the strain ratio ν [17], namely:

$$\nu = \frac{\varepsilon_{h,s}}{\varepsilon_{a,s}}, \tag{4}$$

where $\varepsilon_{h,s}$ is the transverse strain at the position of rectangular stainless steel tube with maximum deformation, and $\varepsilon_{a,s}$ is the longitudinal strain of stainless steel tube.

To study the change laws of strain ratios of the CFRP-confined rectangular CFSST stub columns, the relative load (N/N_u)−strain ratio (ν) curves of the specimens are given in Figs. 6(a)–6(c) (the change laws of square-

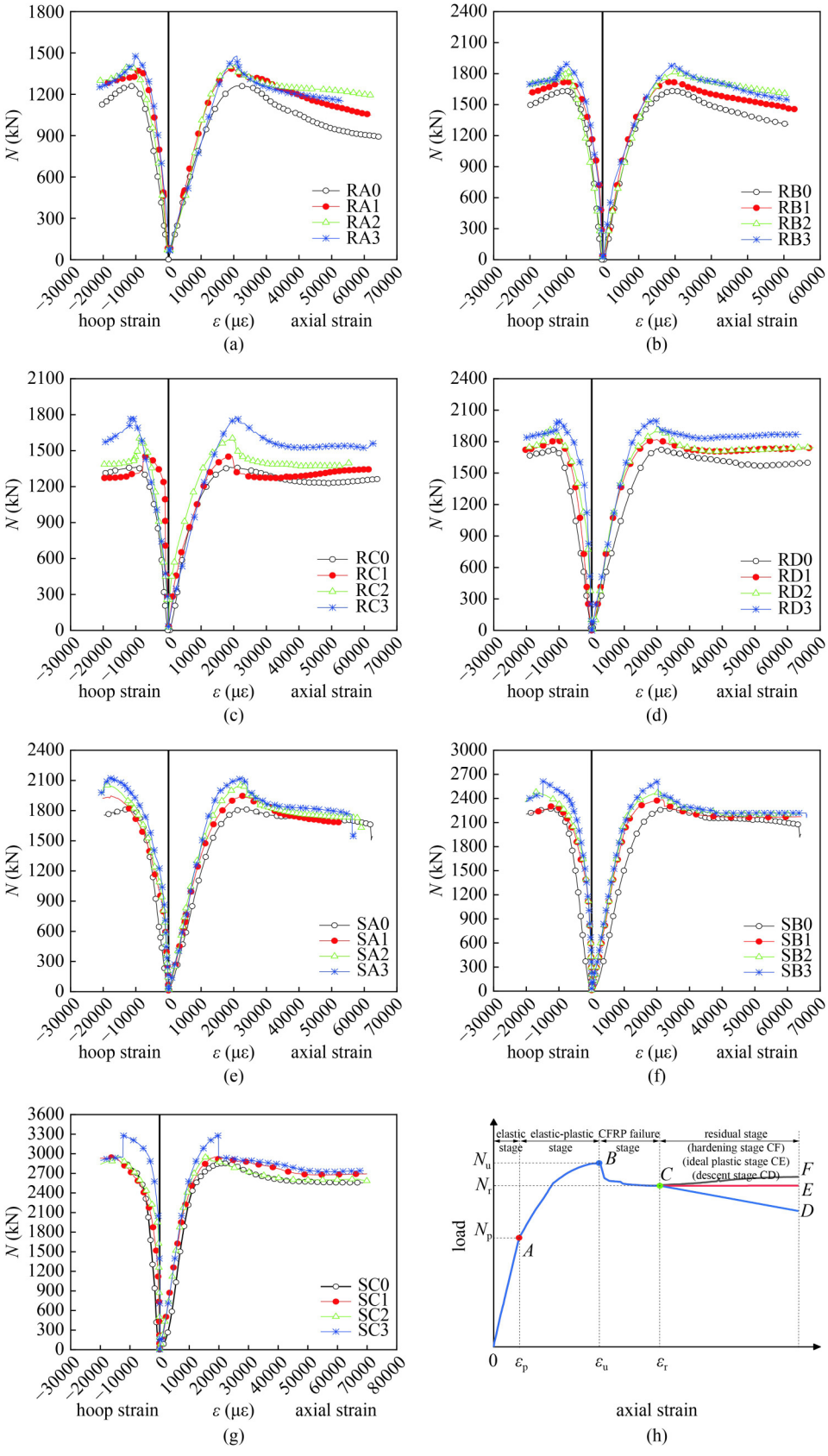

Fig. 5 Load versus strain curves for tested specimens: (a) 120 mm × 60 mm × 4 mm; (b) 120 mm × 60 mm × 5 mm; (c) 120 mm × 80 mm × 4 mm; (d) 120 mm × 80 mm × 5 mm; (e) 120 mm × 120 mm × 4 mm; (f) 120 mm × 120 mm × 5 mm; (g) 120 mm × 120 mm × 6 mm; (h) typical load–longitudinal strain curve.

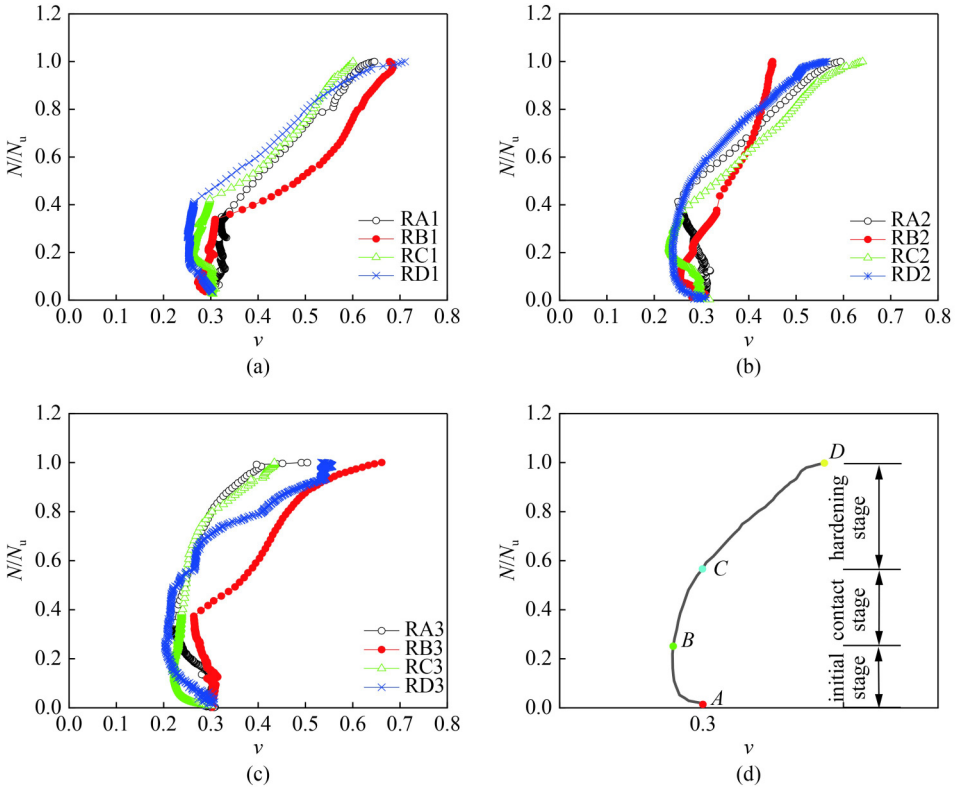

Fig. 6 Relative load (N/N_u)–strain ratio (v) curve: (a) $n_f = 1$; (b) $n_f = 2$; (c) $n_f = 3$; (d) typical N/N_u–v curves.

sectional specimens are identical to those of RD specimens). The typical N/N_u–v curve is displayed in Fig. 6(d), which can be divided into three stages: initial stage (*AB*), contact stage (*BC*), and hardening stage (*CD*).

1) Initial stage (*AB* segment in Fig. 6(d)). In this stage, the initial strain ratio of the specimen is approximately 0.3, which is consistent with the initial Poisson's ratio of stainless steel tube. However, this value is larger than the initial Poisson's ratio (0.2) of core concrete, indicating that the stainless steel tube could not provide constraints for the core concrete and the two bore stresses independently. The transverse deformation of the stainless steel tube was enlarged as the load increased. Meanwhile, the transverse constraint effect of the CFRP on the stainless steel surface increased, while the strain ratio of the stainless steel tube decreased. Stainless steel tubes and concrete independently bore stresses in the initial stage.

2) Contact stage (*BC* stage in Fig. 6(d)). The strain ratio of the stainless steel tube presented a growth trend in this stage. The growth rate of the transverse strain of the steel tube was accelerated with the increase of the load. Meanwhile, the annular tensile stress of CFRP, which was a linear elastic material, was directly proportional to transverse strain, and the constraint effect was not evident under the low-strain condition. Therefore, the strain ratio of the stainless steel tube presented a growth trend. However, the strain ratio of the steel tube slowly increased as the CFRP constraint capability was improved compared with that in the initial stage.

After the initial stage, micro-gaps existed between steel tubes and concrete due to their different transverse deformations. Both independently bore stresses in the contact stage, the core concrete was under the uniaxial compression state. With the increase in load, the stress of the core concrete grew as high as $0.4f_{cu}$, the plastic deformation and microcracks of concrete were further developed, and the Poisson's ratio of the tangent line was enlarged until the transverse deformation of core concrete was completely identical with stainless steel deformation.

3) Hardening stage (*CD* stage in Fig. 6(d)). The stainless steel tube and the concrete were in contact in the contact stage, and the synchronous deformation of the two was present in the hardening stage, and the core concrete was transformed from uniaxial into triaxial compression state. Therefore, the bearing capacity was strengthened significantly. The transverse deformation of the stainless steel tube was further enlarged with the increase in load during this stage. Meanwhile, the transverse deformation and the strain ratio of the steel tube increased due to the extruding effect of internal concrete. However, the growth rate was inhibited to a certain extent by the annular constraint effect of CFRP. The stainless steel tube entered the plastic hardening stage when the load reached $0.96N_u$, and the growth rate of the transverse strain was further accelerated.

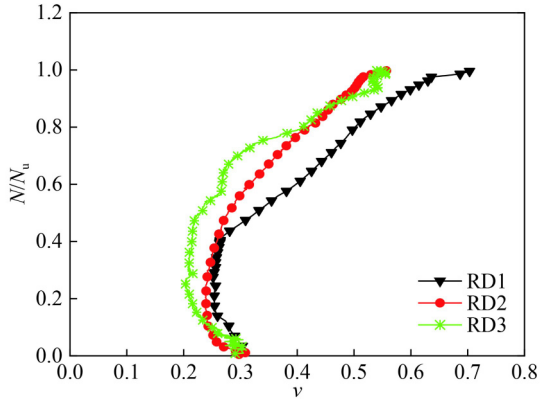

Fig. 7 Relative load (N/N_u)–strain ratio (ν) curve of specimens RD.

The relative load-strain ratio relation curves of the specimens in the RD group, are shown in Fig. 7. The results revealed that the transverse constraint effect of the CFRP on stainless steel tube was enlarged with the increase in the number of CFRP layers. In the initial stage, the larger the steel tube is constrained, the closer the strain ratio of steel tubes to the Poisson's ratio of concrete 0.2, thus the stainless steel tube and concrete can rapidly enter the coordinated deformation stage. Therefore, for the specimens with more CFRP constraints, the load growth rate is faster, and the peak strain is relatively small.

For the specimens without CFRP, the variation trends of the relative load–strain ratio were identical. Therefore, only SC0 specimen was taken, for example (Fig. 8). The strain ratio of the specimen without CFRP was maintained at 0.3 in the initial stage, which was close to Poisson's ratio of stainless steel tube. When the load reached $0.3N_u$, the deformation of the steel tube and the concrete was synchronous due to the steel tube deformation and concrete expansion. Afterward, the strain ratio of the specimen grew rapidly. The growth rate of the strain ratio was further elevated as the load approached $0.9N_u$, and the growth rate was approximately 0.6 under the peak load.

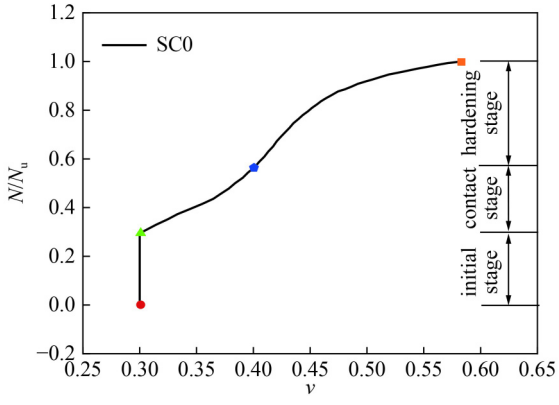

Fig. 8 Relative load (N/N_u)-strain ratio (ν) curve of specimen SC0.

3.4 Influential factors for bearing capacity

The relation curves of stainless steel tube constraint effect coefficients ξ_s and N_u (namely ξ_s–N_u curves) are displayed in Fig. 9. When the length-width ratio and the number of CFRP layers remain unchanged, the greater the steel tube restraint effect, the greater the bearing capacity of the specimen. The bearing capacity of rectangular cross-sectional specimen was related to the length−width ratio (H/B).

The length–width ratio (H/B)−N_u curves are shown in Fig. 10. When the thickness of the steel tube and the number of CFRP layers remain unchanged, namely, when they share the same constraint effect coefficient, the greater the length−width ratio, the weaker the bearing capacity would be. Meanwhile, the bearing capacity of the specimen increased with the increase in the wall thickness of the stainless steel tube when the length−width ratio and n_f remain unchanged.

The influence of the layer of the CFRP on the bearing capacity of rectangular CFSST stub columns was evident, as shown in Fig. 11. The more layers of CFRP, the

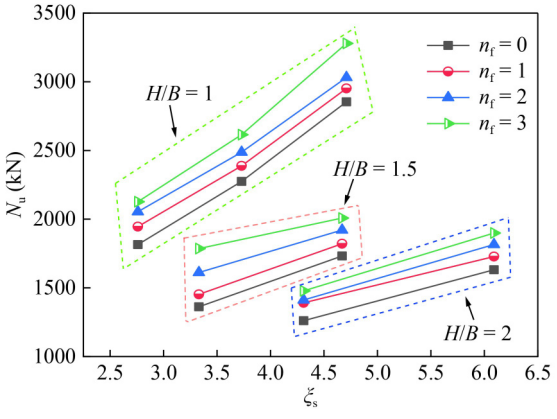

Fig. 9 Effect of ξ_s on N_u.

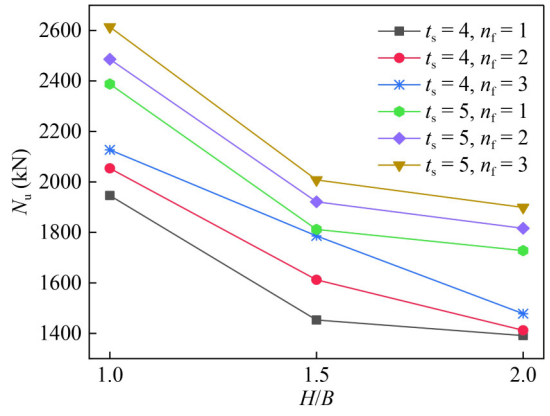

Fig. 10 Effect of H/B on N_u.

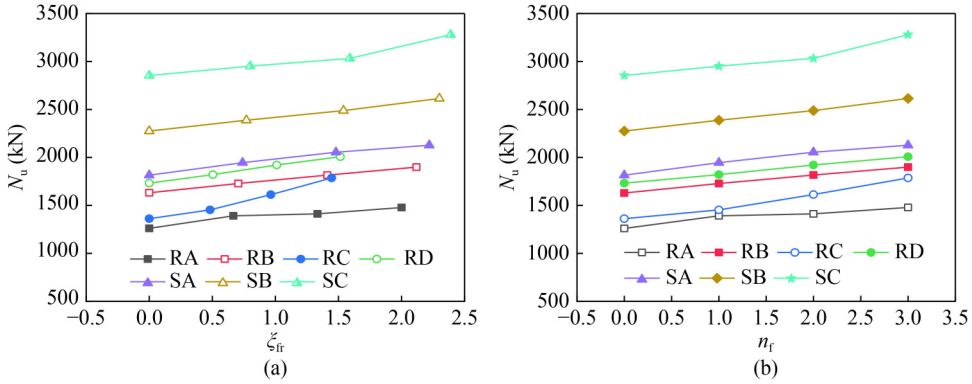

Fig. 11 Effect of CFRP confinement on N_u: (a) effect of ξ_{fr} on N_u; (b) effect of n_f on N_u.

greater the constraint effect of CFRP and the greater the bearing capacity of specimens. Figure 11(b) shows that the bearing capacity of the specimens in the same group is positively correlated with the number of CFRP layers, and the increase ranges at 1–3 layers are approximately 6%, 11%, and 16% of the control specimens.

3.5 Influence of CFRP on specimen ductility

Figure 5 shows that when the CFRP-confined specimens reach the peak load, the load suddenly decreases due to the crack of the CFRP, and then specimens enter the residual stage; the load−strain curves decreased slowly or increased slightly. This phenomenon effectively reflects the specimen ductility and safety, and the load of most specimens does not decline to $0.85N_u$. Therefore, the existing ductility judgment methods for CFRP-confined CFST stub columns, which take DI ($DI = \varepsilon_{85\%}/\varepsilon_y$) as the judgment basis, are inapplicable to CFRP-confined CFSST stub columns.

Referring to the ductility research method proposed by Erfan et al. [23], for rectangular CFSST stub columns, the slope change point on the descent stage of the curve is taken as the reference point for specimen ductility (the point where the load decline to $0.8N_u$), and the ratio of the deformation at this point to the peak load−deformation is used as the ductility criterion. The larger the calculation result is, the better the ductility is. According to the failure characteristics of the CFRP-confined CFSST stub columns, for RA and RB specimens whose curves are in descending stage after CFRP failure, the change point of slope in descending section of the curve is taken as the characteristic point. Meanwhile, for the RC and RD specimens and the SA, SB, and SC specimens with a length-width ratio of 1, the point where the curve starts entering the ascent segment from the steady segment is taken as the feature point (point C), as shown in Fig. 5(h) and Table 4.

For the RA and RB specimens with length−width ratio of 2, their load−strain curves entered the descent segment after the characteristic point; therefore, the greater Δ_1/Δ_u ratio, the better is the ductility. For the other specimens, the load−strain curves of which enter the gentle ascent stage after the characteristic point, the lower the Δ_1/Δ_u ratio means the earlier the specimen curve enters the ascent stage and represents the better ductility. Table 4 shows that the specimen ductility is improved with the growing number of CFRP layers, but the increase in amplitude is small. Meanwhile, the bending failure of the rectangular column occurred easily when the sectional length-to-width ratio is high, while the specimen ductility was reduced. Therefore, it is suggested that the sectional length-to-width ratio should be controlled within 2 in the rectangular stub column design.

Table 4 List of characteristic points of ductility

specimen	Δ_1 (mm)	Δ_u (mm)	Δ_1/Δ_u
RA1	8.93	7.27	1.23
RA2	9.84	7.68	1.28
RA3	10.87	7.95	1.37
RB1	10.43	7.18	1.45
RB2	11.03	7.51	1.46
RB3	11.56	7.81	1.48
RC1	15.28	7.35	2.08
RC2	14.14	7.15	1.98
RC3	14.91	7.66	1.95
RD1	13.61	7.14	1.91
RD2	13.42	7.27	1.85
RD3	12.44	7.32	1.70
SA1	13.28	8.17	1.63
SA2	12.43	8.08	1.54
SA3	10.85	8.16	1.33
SB1	16.42	7.82	2.10
SB2	14.27	7.49	1.91
SB3	13.98	7.34	1.90
SC1	17.30	8.02	2.16
SC2	15.72	5.90	2.66
SC3	16.97	7.15	2.37

Note: Δ_1 represents characteristic point displacement, and Δ_u is peak displacement.

4 Bearing capacity prediction

4.1 Formula of axial compression bearing capacity

According to the calculation method of CECS159:2004 [24] and ACI [25] in calculating the axial compression bearing capacity of rectangular CFST short columns, the bearing capacity of CFSST short columns can be expressed as follows:

$$N_{cr} = A_{s1} f_{a1} + A_{s2} f_{a2} + A_{s3} f_y + A_c f_{cc}, \tag{5}$$

where A_{s1}, A_{s2}, and A_{s3} are the cross-sectional area of the short side plate area, the long side plate area, and the chamfer area, respectively; f_{a1}, f_{a2}, and f_y are the vertical strength of the short side plate area, the long side plate area, and the vertical strength of the chamfer, respectively; A_c and f_{cc} are the cross-sectional area and the axial compressive strength of the core concrete, respectively. f_{cc} can be determined by the mechanical analysis of the specimen in the ultimate equilibrium state based on the unified theory of double shear strength (TUST) [26], which is as follows:

$$\sigma_1 - \frac{\alpha}{1+b}(b\sigma_2 + \sigma_3) = \sigma,\ \sigma_2 \leqslant \frac{\sigma_1 + \alpha\sigma_3}{1+\alpha}, \tag{6}$$

$$\frac{1}{1+b}(\sigma_1 + b\sigma_2) - \alpha\sigma_3 = \sigma,\ \sigma_2 \geqslant \frac{\sigma_1 + \alpha\sigma_3}{1+\alpha}, \tag{7}$$

where σ_1, σ_2, and σ_3 are principal stresses in three directions respectively; b is a weighted parameter, and α is the ratio of tensile strength to the compressive strength of the material.

4.2 Effective confining pressure of core concrete

The effective confining pressures of the long and short sides of stainless steel tube on the core concrete are calculated by Eqs. (8) and (9), respectively, which are based on the method of confining pressures of the confined concrete proposed by Mander et al. [27]:

$$f_{l1} = k_e f'_{l1}, \tag{8}$$

$$f_{l2} = k_e f'_{l2}, \tag{9}$$

where k_e is the effective constraint coefficient of the core concrete; and f_{l1} are f_{l2} the effective confining pressure of the short side plate and the long side plate on the core concrete, respectively; and f'_{l1} are f'_{l2} the lateral confining stress along the short side plate and the long side plate caused by the stainless steel tube.

The force analysis of the stainless steel tube is shown in Fig. 12, and it is assumed that the long and short sides of the stainless steel tube are under uniform confining pressure in the limiting equilibrium state. The ideal confining pressure is calculated by Eqs. (10) and (11):

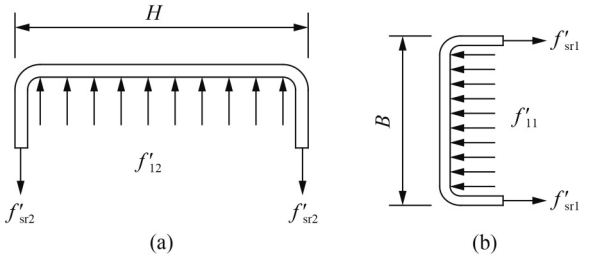

Fig. 12 Sketch map of lateral forces on rectangular stainless steel tube: (a) long side; (b) short side.

$$f'_{l1} = \frac{2f'_{sr1}t_s}{B - 2t_s}, \tag{10}$$

$$f'_{l2} = \frac{2f'_{sr2}t_s}{H - 2t_s}, \tag{11}$$

where f'_{sr1} and f'_{sr2} are the lateral tensile stresses of the long and short sides of the stainless steel tube, respectively.

4.2.1 Lateral tensile stress of rectangular stainless steel tube

The rectangular stainless steel tube is assumed to be in-plane stress state [28,29] and yields to von Mises criterion. According to the yield criterion, the following Eqs. (12) and (13) can be obtained.

$$f_{a1}^2 - f_{a1}f'_{sr1} + f'^2_{sr1} = f_y^2, \tag{12}$$

$$f_{a2}^2 - f_{a2}f'_{sr2} + f'^2_{sr2} = f_y^2. \tag{13}$$

According to Ref. [30] about the influence of the width-to-thickness ratio (R) on the failure mode of concrete-filled square steel tube, the width-to-thickness ratio R_1 and R_2 of the short and long sides of rectangular stainless steel tube are defined as follows:

$$R_1 = \frac{B}{t_s}\sqrt{\frac{12(1-\upsilon^2)}{4\pi^2}}\sqrt{\frac{f_y}{E_0}}, \tag{14}$$

$$R_2 = \frac{H}{t_s}\sqrt{\frac{12(1-\upsilon^2)}{4\pi^2}}\sqrt{\frac{f_y}{E_0}}, \tag{15}$$

where υ and E_0 are the Poisson's ratio and initial elastic modulus of stainless steel tube, respectively, and f_y is the vertical strength of the stainless steel tube. Since the stainless steel strain is greater than 0.2% of the theoretical

residual strain when the strength of the specimen reaches the peak, it has entered the plastic hardening stage. The strength strengthening effect is considered at this stage, namely, $f_y = k_{ss}\sigma_{0.2}$.

The local buckling failure occurs at the short side of the rectangular stainless steel tube when R_1 is greater than 0.85 [30,31], and $f_{a1} = f_b$. f_b is the local buckling strength of the stainless steel tube, which is determined by Eq. (16). When f_b is greater than 0.89 f_y, 0.89 f_y is adopted, and f_{sr1} is equal to $-0.19f_y$.

$$f_b = \left(\frac{1.2}{R_1} - \frac{0.3}{R_1^2}\right) f_y, \tag{16}$$

$$f_{sr1} = \frac{f_{a1} - \sqrt{4f_y^2 - 3f_{a1}^2}}{2}. \tag{17}$$

Otherwise, when R_1 is less than 0.85, the effects of local buckling can be ignored. In this case, f_{a1} and f_{sr1} are equal to $0.89f_y$ and $-0.19f_y$, respectively [30].

Similarly, when $R_2 > 0.85$, the equation of $f_{a2} = f_b$ exists. In this case, it is considered that local buckling failure occurs on the long side of rectangular stainless steel tube, and f_b is determined by the following Eq. (18).

$$f_b = \left(\frac{1.2}{R_2} - \frac{0.3}{R_2^2}\right) f_y, \tag{18}$$

$$f_{sr2} = \frac{f_{a2} - \sqrt{4f_y^2 - 3f_{a2}^2}}{2}. \tag{19}$$

If the value of f_b from Eq. (18) is greater than $0.89f_y$, $f_b = 0.89f_y$, and $f_{sr1} = -0.19f_y$.

When $R_1 \leqslant 0.85$, the value of f_{sr2} and f_{a2} are equal to $0.89f_y$ and $-0.19f_y$, respectively [30].

4.2.2 Effective constraint coefficient of core concrete

The effective constraint coefficient k_e of the core concrete can be determined by Eq. (20) [27].

$$k_e = k_{e1}k_{e2}, \tag{20}$$

where k_{e1} and k_{e2} are the cross-sectional confinement coefficient and the axial confinement coefficient, respectively. Since the constraint effect of the stainless steel tube on the core concrete is continuous along the axial direction, k_{e2} equals to 1. For the cross-sectional confinement coefficient k_{e1}, a relationship proposed by Mander et al. [27] is applied herein.

$$k_{e1} = \frac{A_e}{A_c}, \tag{21}$$

where A_e is the horizontal area of an effectively confined core concrete. Referring to the analysis method in Ref. [32] for axial compressive performance of special-section multi-cavity CFST columns, it is assumed that the boundary line of the effective constraint zone of core and concrete is a quadratic parabola, and the tangent angles of the constraint boundary are θ_1 and θ_2, respectively (Fig. 13), and the following can be obtained:

$$A_e = (B - 2t_s)(H - 2t_s) - 2A_1 - 2A_2, \tag{22}$$

$$A_1 = \frac{(B - 2t_s)^2 \tan\theta_1}{6}, \tag{23}$$

$$A_2 = \frac{(H - 2t_s)^2 \tan\theta_2}{6}, \tag{24}$$

$$k_{e1} = 1 - \frac{(B - 2t_s)\tan\theta_1}{3(H - 2t_s)} - \frac{(H - 2t_s)\tan\theta_2}{3(B - 2t_s)}, \tag{25}$$

where A_1 and A_2 are the area of the constraint regions (the shaded part in Fig. 13). Long and Cai [31] suggested that θ_1 and θ_2 are 23°.

Referring to the calculation method of the equivalent lateral constraint of stirrup confined concrete proposed by Mander et al. [27] and based on the principle of equal area, the rectangular cross-section of the stainless steel tube concrete short column is transformed into a circular cross-section. The simplified stress model of the stainless steel tube is shown in Fig. 14.

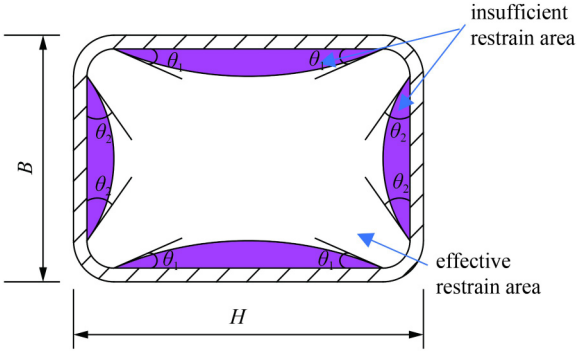

Fig. 13 Effectively confined concrete core of cross-section.

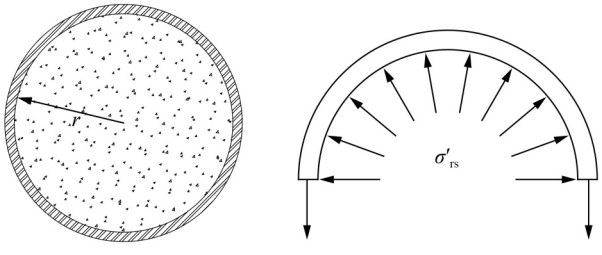

Fig. 14 Stress diagram of equivalent round steel tube.

The confining pressure on the long and short sides of the rectangular steel pipe is evenly distributed on the inner surface of the equivalent circular section steel pipe, and the equivalent confining pressure σ'_{rs} is calculated by Eq. (26).

$$\sigma'_{rs} = \frac{k_e\left[f_{l1}(B-2t_s)+f_{l2}(H-2t_s)\right]}{\pi r}, \tag{26}$$

$$r = \sqrt{(B-2t_s)(H-2t_s)/\pi}. \tag{27}$$

The confining pressure of core concrete (σ_{rs}) is equal to σ'_{rs}.

4.2.3 Axial compression bearing capacity

According to the above equivalent method, the equivalent stress analysis of the core concrete is shown in Fig. 15, where $\sigma_1 = \sigma_2 = \sigma_{rs}$. Substitute it into TUST [32], and the following can be obtained:

$$f_{cc} = \sigma_3 = f_c + k\gamma_u\sigma_{rs}, \tag{28}$$

$$\gamma_u = 1.67 \times D^{-0.112}, \tag{29}$$

$$k = (1+\sin\varphi)/(1-\sin\varphi), \tag{30}$$

$$D = 2r, \tag{31}$$

where γ_u is the reduction coefficient of the concrete strength [33], k is the coefficient of horizontal pressure, where ϕ is the internal friction angle of the concrete, and $\varphi = 30°$ [34].

Therefore, the ultimate bearing capacity of rectangular CFSST short column can be expressed as follow:

$$N_{cr} = A_{s1}f_{a1} + A_{s2}f_{a2} + k_{ss}A_{s3}\sigma_{0.2} + A_c f_c + A_c k\gamma_u \frac{k_e\left[f_{l1}(B-2t_s)+f_{l2}(H-2t_s)\right]}{\sqrt{\pi(B-2t_s)(H-2t_s)}}. \tag{32}$$

The experimental data in this paper and the relevant literature data were substituted into Eq. (32), and $k_{ss} = 1.24$ was determined by data fitting. The calculation and test values of bearing capacity are presented in Table 5 and Fig. 16. Generally, the errors between the calculation and test value in this paper are 10%, and some errors are relatively large due to the big difference in the strength of steel tube confined concrete.

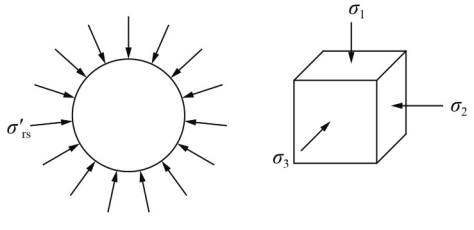

Fig. 15 Stress state of the core concrete.

4.3 Axial compressive capacity of FRP-confined CFSST

Figure 17 presents the influence of the CFRP constraint effect on the bearing capacity of CFSST. The relationship between ξ_{fr}/ξ_s and the strengthening degree η_{fr} of the specimen bearing capacity η_{fr} is obtained through the numerical fitting method.

When $H/B = 1.0$,

$$\eta_{fr} = (0.24353 + 23.11729\xi_{fr}/\xi_s) \times 100\%. \tag{33}$$

When $H/B \geqslant 1.5$,

$$\eta_{fr} = (0.23575 + 50.41778\xi_{fr}/\xi_s) \times 100\%. \tag{34}$$

Hence, the recommended calculation formula for the axial compression bearing capacity of the CFRP-constrained rectangular CFSST stub columns is as follows:

$$N_{cfr} = \eta_{fr}N_{cr}. \tag{35}$$

Equation (35) is used to calculate the bearing capacity of test specimens in this paper, and N_{cfr}/N_u statistical graph is shown in Fig. 18. The calculated values are close to the experimental values, and the errors are mostly within 8% and are less than the experimental values, indicating that the above equation can better predict the axial compression bearing capacity of CFRP-constrained CFSST short column and has certain safety margin.

The H/B–N_i/N_j curves are presented in Fig. 19, where N_j is the bearing capacity of the CFRP-constrained CFSST stub columns in the same batch with square sections, and N_i is the corresponding bearing capacity of the CFRP-constrained CFSST stub columns with the same wall thickness, the number of CFRP layers, and concrete strength and different length-width ratios. The specimen bearing capacity decreases with the growth of H/B, a largely second-order nonlinear relation is manifested, and the nonlinear relation between H/B and N_i/N_j is obtained through numerical fitting.

$$\frac{N_i}{N_j} = 1.91 - 1.22H/B + 0.31(H/B)^2. \tag{36}$$

As the section considerably influences the stainless steel material strength, the rectangular steel tubes with the same wall thickness but different length–width ratios will be different in yield strength. Therefore, if the bearing capacity of square CFSST is known and the yield strength of rectangular steel tubes is unknown, Eq. (36) can be used to calculate the predicted bearing capacity of rectangular CFSST with length-to-width ratio of 1–2.

Table 5 Calculation and test values of bearing capacity

specimen	B (mm)	H (mm)	t_s (mm)	R_c (mm)	E_0 (GPa)	υ	$\sigma_{0.2}$ (MPa)	f_{ck} (MPa)	N_u (kN)	N_{cr} (kN)	N_{cr}/N_u	Ref. No
120 × 60 × 4-0	60	120	4	4	195	0.3	538	33.44	1261	1184	0.94	this paper
120 × 60 × 5-0	60	120	5	5	200	0.3	581	33.44	1632	1522	0.93	
120 × 80 × 4-0	80	120	4	4	196	0.3	516	33.44	1362	1338	0.98	
120 × 80 × 5-0	80	120	5	5	200	0.3	558	33.44	1732	1705	0.98	
120 × 120 × 4-0	120	120	4	4	203	0.3	549	33.44	1815	1788	0.99	
120 × 120 × 5-0	120	120	5	5	203	0.3	578	33.44	2275	2210	0.97	
120 × 120 × 6-0	120	120	6	6	203	0.3	592	33.44	2854	2614	0.92	
150 × 150 × 6C40	150	150	6	6	194	0.3	497	35.4	2768	3005	1.08	[16]
150 × 150 × 6C60	150	150	6	6	194	0.3	497	47.05	2972	3231	1.08	
100 × 100 × 5C30	100	100	5	5	180	0.3	458	22.8	1410	1383	0.98	[35]
100 × 100 × 5C60	100	100	5	5	180	0.3	458	40.28	1488	1527	1.03	
100 × 100 × 5C100	100	100	5	5	180	0.3	458	56.24	1559	1658	1.06	
50 × 50 × 2C20	50	50	2	2	205.1	0.3	353	16.3	261	221	0.85	[17]
50 × 50 × 2C30	50	50	2	2	205.1	0.3	353	26.5	282	242	0.86	
50 × 50 × 3C20	50	50	3	3	202.9	0.3	440	16.3	417	381	0.91	
100 × 100 × 3C20	100	100	3	3	195.7	0.3	358	16.3	716	703	0.98	
100 × 100 × 3C30	100	100	3	3	195.7	0.3	358	26.5	757	793	1.05	
100 × 100 × 5C20	100	100	5	5	195.7	0.3	435	16.3	1449	1270	0.88	
100 × 100 × 5C30	100	100	5	5	195.7	0.3	435	26.5	1490	1352	0.91	
150 × 150 × 3C20	150	150	3	3	192.6	0.3	268	16.3	1062	962	0.91	
150 × 150 × 3C30	150	150	3	3	192.6	0.3	268	26.5	1209	1173	0.97	
150 × 150 × 5C20	150	150	5	5	192.6	0.3	340	16.3	1935	1641	0.85	
150 × 150 × 5C30	150	150	5	5	192.6	0.3	340	26.5	2048	1840	0.90	
304-t8c50	295.52	295.52	7.75	7.75	196.6	0.3	293	36.6	6290	6277	1.00	[36]
304-t10c50	300	300	9.87	9.87	196.2	0.3	287	36.6	7113	7212	1.01	
304-t12c50	303.74	303.74	11.87	11.87	199.4	0.3	301	36.6	7924	8411	1.06	
304-t8c70	295.52	295.52	7.75	7.75	196.6	0.3	293	54.5	6743	7692	1.14	
304-t10c70	300	300	9.87	9.87	196.2	0.3	287	54.5	7947	8589	1.09	
304-t12c70	303.74	303.74	11.87	11.87	199.4	0.3	301	54.5	8575	9788	1.14	
304-t8c80	295.52	295.52	7.75	7.75	196.6	0.3	293	62.4	7436	8309	1.12	
304-t10c80	300	300	9.87	9.87	196.2	0.3	287	62.4	8430	9204	1.09	
304-t12c80	303.74	303.74	11.87	11.87	199.4	0.3	301	62.4	9257	10402	1.12	

5 Conclusions

1) The failure mode of the CFRP-confined rectangular concrete-filled stainless steel tube stub columns is described as follows. First, the local rupture of CFRP occurred, and the local buckling failure of the concrete-filled stainless steel tube was present. The bearing capacity of the CFRP-confined concrete-filled stainless steel tube stub columns was stronger than that of concrete-filled stainless steel tube specimens because of the strong restraint capacity of CFRP. Following the CFRP ruptured, the typical load−longitudinal strain curves of the specimens presented three different development trends due to the different constraint effects of stainless steel.

2) The local buckling of stainless steel tubes decreased, and the bearing capacity of concrete-filled stainless steel tube stub columns increased due to the CFRP. The bearing capacity of the CFRP-confined specimens was slightly stronger than that of the specimens without the CFRP.

3) The bearing capacity of the CFRP-confined rectangular concrete-filled stainless steel tube stub columns was substantially influenced by the CFRP

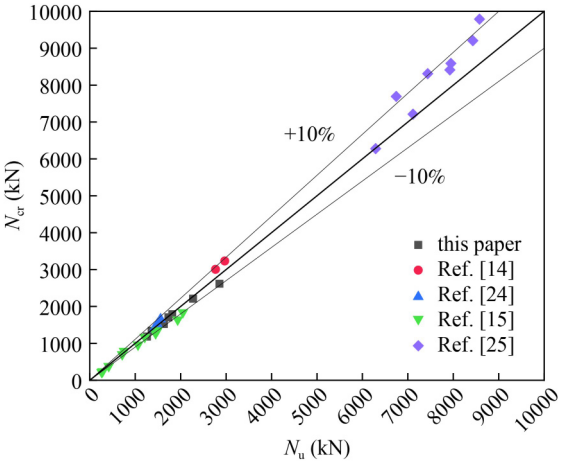

Fig. 16 Comparison diagram of calculated and test values.

constraint effect coefficient, sectional length−width ratio, and the thickness of the steel tube. Specifically, the bearing capacity increased with the number of CFRP layers, declined with the increase in sectional length-width ratio, and decreased as the steel tube thickness increased.

4) The CFRP-confined rectangular concrete-filled stainless steel tube stub columns had favorable ductility. By analyzing the characteristics of load–strain curves of CFRP-CFSST, a ductility discrimination method is proposed, which takes the change point of the slope of residual stage curve as the characteristic point.

5) The recommended calculation formulas for the bearing capacity of rectangular concrete-filled stainless steel tube stub columns and the bearing capacity of CFRP-confined rectangular concrete-filled stainless steel tube stub columns were obtained through numerical fitting. The prediction formula for the bearing capacity considering the sectional effect was obtained as well. This formula is of high accuracy with a certain safety margin.

Acknowledgements This study was generously funded by the National Natural Science Foundation of China (Grant No. 51268044). The first author also appreciates the support from the University of Pittsburgh and North Dakota State University when he worked as a visiting scholar.

Notations

A_c: cross-sectional area of core concrete

A_{cfst}: total cross-sectional area of carbon steel tube and core concrete

A_{fr}: cross-sectional area of CFRP wrap

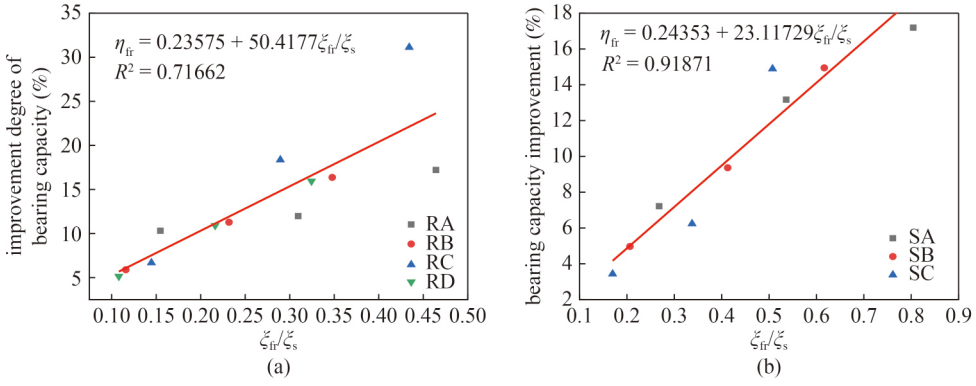

Fig. 17 Influence of ξ_{fr}/ξ_s on the lifting degree of bearing capacity: (a) $H/B \geqslant 1.5$; (b) $H/B = 1.0$.

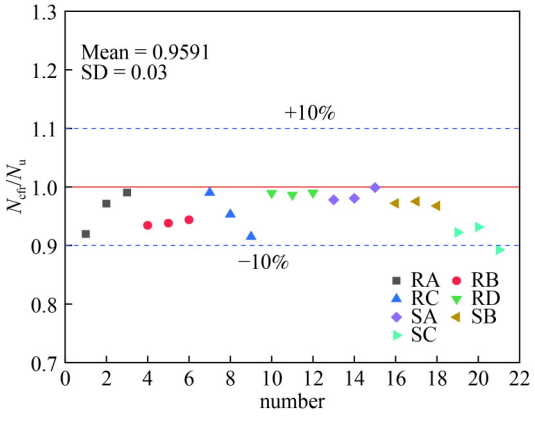

Fig. 18 Statistics graph of N_{cfr}/N_u.

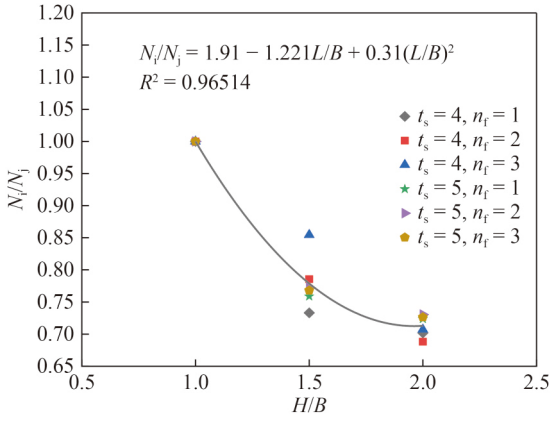

Fig. 19 The effect of H/B on the bearing capacity of CFRP constrained specimens.

A_s: cross-sectional area of stainless steel tube
B: short side of rectangular steel tube
DI: ductility index
E_0: elastic modulus of stainless steel
E_{fr}: elastic modulus of CFRP sheet
H: specimen height
f_{ck}: vcharacteristic strength of concrete
f_{cu}: standard cubic compressive strength of concrete
f_{cfst}: strength index of concrete in rectangular stainless steel tube under axial compression
f_{fr}: tensile strength of CFRP sheet
L: long side of rectangular steel tube
n: hardening exponent of stainless steel
n_f: number of CFRP layers
N: load
N_{cfr}: predicted load-carrying capacity
N_{cfst}: bearing capacity of concrete-filled stainless steel tubular stub columns with rectangular section under axial compression
N_{cr}: calculation value of ultimate bearing capacity of concrete-filled rectangular stainless steel tubular short columns
N_p: proportional limit load
N_r: residual load capacity of the FRP-confined CFSST after full fracture of CFRP wrap
N_u: peak load at failure
t_{fr}: CFRP thickness
t_s: wall thickness of stainless steel tube
Δ: axial deformation
Δ_1: axial deformation corresponding to the feature point
Δ_u: axial deformation corresponding to ultimate strength
$\varepsilon_{85\%}$: axial strain when the load falls to 85% of the ultimate load
ε: strain of stainless steel
$\varepsilon_{a,s}$: longitudinal strain
$\varepsilon_{h,s}$: transverse strain
ε_y: $\varepsilon_{75\%}/0.75$, where $\varepsilon_{75\%}$ is the axial strain when the load attains 75% the ultimate load in the pre-peak stage
ε_p: corresponding axial strain of proportional limit load
ε_r: corresponding axial strain of the lowest point at failure
ε_u: corresponding axial strain of the peak load at failure
η_{fr}: improvement of specimen bearing capacity
ϕ: sectional stability coefficient
ν: lateral-to-axial strain ratio
$\sigma_{0.2}$: 0.2% proof stress of stainless steel
ξ_{fr}: confinement factor of CFRP wrap
ξ_s: confinement factor of stainless steel tube
υ: Poisson's ratio

References

1. Ozbakkaloglu T, Oehlers D J. Manufacture and testing of a novel FRP tube confinement system. Engineering Structures, 2008, 30(9): 2448−2459
2. Marques S P C, Marques D C D S C, Lins da Silva J, Cavalcante M A A. Model for analysis of short columns of concrete confined by fiber-reinforced polymer. Journal of Composites for Construction, 2004, 8(4): 332−340
3. Jiang T, Teng J G. Analysis-oriented stress–strain models for FRP-confined concrete. Engineering Structures, 2007, 29(11): 2968−2986
4. Masia M J, Gale T N, Shrive N G. Size effects in axially loaded square-section concrete prisms strengthened using carbon fibre reinforced polymer wrapping. Canadian Journal of Civil Engineering, 2004, 31(1): 1−13
5. Guo Y C, Xiao S H, Luo J W, Ye Y Y, Zeng J J. Confined concrete in fiber-reinforced polymer partially wrapped square columns: Axial compressive behavior and strain distributions by a particle image velocimetry sensing technique. Sensors (Basel), 2018, 18(12): 4118
6. Wang Y F, Wu H L. Size effect of concrete short columns confined with aramid FRP jackets. Engineering Structures, 2011, 15(4): 535−544
7. Ozbakkaloglu T. Behavior of square and rectangular ultra high-strength concrete-filled FRP tubes under axial compression. Composites Part B:Engineering, 2013, 54: 97−111
8. Yang J L, Lu S W, Wang J Z, Wang Z. Behavior of CFRP partially wrapped square seawater sea-sand concrete columns under axial compression. Engineering Structures, 2020, 222: 111119
9. Tao Z, Han L H, Zhuang J P. Using CFRP to strengthen concrete-filled steel tubular columns: Stub column tests. In: Fourth International Conference on Advances in Steel Structures. Shanghai: Elsevier Science Ltd, 2005, 701–706
10. Tao Z, Han L H, Zhuang J P. Axial loading behavior of CFRP strengthened concrete-filled steel tubular stub columns. Advances in Structural Engineering, 2007, 10(1): 37−46
11. Wang Y, Cai G, Larbi A S, Waldmann D, Tsavdaridis K D, Ran J. Monotonic axial compressive behaviour and confinement mechanism of square CFRP-steel tube confined concrete. Engineering Structures, 2020, 217: 110802
12. Dong J F, Wang Q Y, Guan Z W. Structural behaviour of recycled aggregate concrete filled steel tube columns strengthened by CFRP. Engineering Structures, 2013, 48: 532−542
13. Sundarraja M C, Prabhu G G. Experimental study on CFST members strengthened by CFRP composites under compression. Journal of Constructional Steel Research, 2012, 72: 75−83
14. Zhou F, Fang C, Chen Y S. Experimental and numerical studies on stainless steel tubular members under axial cyclic loading. Engineering Structures, 2018, 171: 72−85
15. Fang C, Zhou F, Luo C H. Cold-formed stainless steel RHSs/SHSs under combined compression and cyclic bending. Journal of Constructional Steel Research, 2018, 141: 9−22
16. Young B, Ellobody E. Experimental investigation of concrete-filled cold-formed high strength stainless steel tube columns. Journal of Constructional Steel Research, 2006, 62(5): 484−492
17. Uy B, Tao Z, Han L H. Behaviour of short and slender concrete-filled stainless steel tubular columns. Journal of Constructional Steel Research, 2011, 67(3): 360−378
18. Ibañez C, Hernandez-Figueirido D, Piquer A. Shape effect on axially loaded high strength CFST stub columns. Journal of Constructional Steel Research, 2018, 147: 247−256
19. Tang H Y, Chen J L, Fan L Y, Sun X J, Peng C M. Experimental investigation of FRP-confined concrete-filled stainless steel tube stub columns under axial compression. Thin-walled Structures,

2020, 146: 106483
20. GB/T228.1–2010. Tensile Testing of Metallic Materials Part 1: Room Temperature Test Method. Beijing: General Administration of Quality Supervision, inspection and Quarantine of the People's Republic of China, 2010 (in Chinese)
21. GB/T50080–2016. Standard for Performance Test Method of Ordinary Concrete Mixture. China Construction Industry Press: Ministry of Housing and Urban Rural Development of the People's Republic of China, 2016 (in Chinese)
22. Tang H Y, Deng X Z, Lin Z B, Zhou X. Analytical and experimental investigation on bond behavior of CFRP-to-stainless steel interface. Composite Structures, 2019, 212: 94−105
23. Erfan A M, Ahmed H H, Mina B A, El-Sayed T A. Structural performance of eccentric ferrocement RC columns. Nanoscience and Nanotechnology Letters, 2019, 11: 1−13
24. CECS 159: 2004. Technical Specification for Structures with Concrete-filled Rectangular Steel Tube Members. China planning Press: China Association for Engineering Construction Standardization, 2004
25. ACI 318. Building Code Requirements for Reinforced Concrete and Commentary. Detroit: American Concrete Institute, 2005
26. Yu M H. Unified Strength theory and Its Applications. Berlin, Heidelberg: Springer Press, 2004
27. Mander J A B, Priestley M J N, Park R. Theoretical stress−strain model for confined concrete. Journal of Structural Engineering, 1988, 114(8): 1804−1826
28. Zhong S T. Concrete Filled Steel Tube Structures. 3rd ed. Beijing: Tsinghua University Press, 2003 (in Chinese)
29. Shanmugam N E, Lakshmi B. State of the art report on steel-concrete composite columns. Journal of Constructional Steel Research, 2001, 57(10): 1041−1080
30. Ge H B, Usami T. Strength analysis of concrete filled thin-walled steel box columns. Journal of Constructional Steel Research, 1994, 30(3): 259−281
31. Long Y L, Cai J. Stress–strain relationship of concrete confined by rectangular steel tubes with binding bars. Journal of Constructional Steel Research, 2013, 88: 1−14
32. Wu H P, Cao W L, Dong H Y. Axial compressive strength calculation based on the 'unified theory' for special-shaped CFT columns with multiple cavities. Engineering Mechanics, 2019, 36(8): 114−121 (in Chinese)
33. Sakino K, Nakahara H, Morino S, Nishiyama I. Behavior of centrally loaded concrete-filled steel-tube short columns. Journal of Structural Engineering, 2004, 130(2): 180−188
34. Wei J, Zhao J H, Liu Y D, Tian H W. Analysis of ultimate bearing capacity of concrete-filled steel tubular axial compression short columns. Journal of Architecture and Civil Engineering, 2008, 25(3): 81−86 (in Chinese)
35. Lam D, Gardner L. Structural design of stainless steel concrete filled columns. Journal of Constructional Steel Research, 2008, 64(11): 1275−1282
36. Dai P, Yang L, Wang J. Experimental study on bearing behavior of concrete-filled square stainless steel tube stub columns under axial. Journal of Building Structures, 2021, 42(6): 182−189 (in Chinese)